Suporting Information for

A Pre-fatigue Training Strategy to Stabilize $LiCoO_2$ at High Voltage

Siyuan Qi[a,b], Yujia Guan[a], Junjun Wang[a], Rui Xia[b], Lei Zhang*[a,b,d], Jinghao Li[a], Congli Sun*[a], Qinyou An[a,b,d], and Kangning Zhao*[e]

[a] State Key Laboratory of Advanced Technology for Materials Synthesis and Processing, Wuhan University of Technology, Wuhan, 430070, P. R. China.

*E-mail: zhanglei1990@whut.edu.cn; conglisun@whut.edu.cn.

[b] The Sanya Science and Education Innovation Park of Wuhan University of Technology, Sanya, 572000, P. R. China

[c] Beijing Huichu Technology Co., Ltd., Fengtai District, Beijing, 100038, China

[d] Hubei Longzhong Laboratory, Xiangyang, Hubei, 441000，China

[e] Laboratory of Advanced Separations, École polytechnique fédérale de Lausanne, Sion, 1950, Switzerland

*E-mail: kangning.zhao@epfl.ch.

Experimental Section

Materials preparation

300 mg of commercial $LiCoO_2$ powder was first grounded in an agate mortar and dried at 120 °C for 12h. The samples were evenly spread into a plasma quartz reactor. The plasma experimental power supply is CTP-2000K produced by Nanjing Suman Plasma Technology Co. The sample was placed in a low temperature plasma atmospheric pressure gas-solid reactor DBD 100A. The discharge surface diameter was 50 mm, the discharge distance was 8 mm, and the sample spread thickness was 0.1mm. The plasma chamber is shown in **Figure S1**. The commercial $LiCoO_2$ powder was treated in a sequence of oxygen, argon, and oxygen, with the power of 120 W, and the treatment time of 90 s in each atmosphere, to obtain the OAO-LCO samples (**Figure S2**).

Electrochemical characterizations

Electrochemical measurements for half cells were performed via CR2016 coin-type cells, a metal lithium plate as the counter electrode and the $LiPF_6$ (1.2 mol L^{-1}) dissolved in ethylene carbonate (EC), ethyl methyl carbonate (EMC) (EC: EMC=3:7) , and 2 wt % Vinylene Carbonate (VC) as an additive as the electrolyte. The active material was mixed with super P carbon and poly (vinylidene fluoride) (PVDF) (mass ratio is 8:1:1), and dissolved in N-methyl pyrrolidinone (NMP) to obtain the composite electrode slurry, then the slurry was uniformly applied to Al foil and dried overnight at 120°C for 15 h. The loaded mass of the active materials is about 3.0 – 20 mg cm^{-2}. For the full coin cells, the negative electrode was composed of 90 wt% graphite, 5wt% Super P, 2wt% carboxymethylcellulose (CMC) sodium and 3wt% Styrene-butadiene rubber (SBR). The positive electrode consisted of 90 wt% LCO, 5 wt% Super P, and 5 wt% PVDF. The capacity ratio of negative to positive electrode (N/P ratio) is 1.05. CR2016 coin cells were fabricated in an Ar gas glove box. Using an automatic galvanostat (LAND CT2001A) to test the galvanostatic charge-discharge cycles capacity at 3.0–4.6 V versus Li^+/Li and Li^+/ graphite. The CV and EIS test was carried out using a ZIVE-MP2A. GITT measurements were tested during the first cycle with a titration step at 0.1 C of the 1800s and a relaxation step of 36,000 s. To evaluate room-temperature OER activity in aqueous solutions, electrocatalytic measurements were performed in a three-electrode cell using a glassy carbon electrode (diameter: 3 mm). Calomel electrode was used as the reference electrode. was used as the reference electrode. Graphite rod was used as the counter electrode. 0.1 M KOH aqueous solution with continuous O_2 bubbling was used as the electrolyte. To prepare the testing materials loaded electrodes, 5 mg active materials (P-LCO, or OAO-LCO) and 5 mg carbon black were dispersed in 1 ml Nafion/alcohol solution (0.5

wt%) under ultrasound and stirred for 4 h to obtain a homogenous ink and 10 µl ink were coated on the glassy carbon electrode. Linear sweep voltammetry was conducted at 5 mV s^{-1}.

Characterization techniques

Powder X-ray diffraction was performed on a diffractometer (Rigaku, CuKα) in the 2θ range of 10°-80° with a step width of 0.01°. The lattice parameters were refined using Fullprof software based on the Rietveld method. The In situ and X-ray diffraction was carried out on the X-ray diffractometer (XRD, Rigaku, CuKα) in the 2θ range of 10°−50° with a step with of 0.01° and a scan rate of 20°/min. Scanning electron microscopy (SEM, Phenom) was applied to observe the microstructures of the samples. SEM images were collected using a JEOL-7100F scanning electron microscope. The TEM/STEM images, EELS/EDX spectra, and electron tomography experiments were collected using a CEOS probe corrected FEI Themis TEM instrument (electron accelerating voltage of 300kV) equipped with a Gatan image filter spectrometer. The probe convergence angle was 17.8 mrad, and the probe current was ~45pA for STEM imaging and EELS/EDS acquisition. EELS was performed with a Gatan Quantum 965 GIF system. Dual EELS was recorded for simultaneous visualization of zero loss and Ti M, Li K, and Ti L edges for calibration. The energy resolution was ~0.9 eV, which was determined by the full width at half-maximum of the zeroloss peak. X-ray photoelectron spectroscopy (XPS) were carried out using an ESCALAB 250Xi instrument and depth profiles were obtained by assisted Ar^+ etching. Typically the hydrocarbon C *1s* line at 284.8eV from adventitious carbon is used for energy referencing. Electron paramagnetic resonance (EPR) spectra were obtained with a Bruker Elexsys E500-T spectrometer with a liquid nitrogen cryostat at 100 K. EPR acquisition parameters are as follow: microwave frequency of 9.42 GHz, microwave power of 1 mW (23 dB), modulation amplitude of 2 gauss, conversion time of 81.92 ms, time constant of 40.96 ms. Height and Young's modulus of LCO and conductivity of cathode were collected using an AFM (Dimension ICON, US) via c-AFM with an SCM-PIT-V2 probe. The electrode surface was used TOF-SIMS (PHInanoTOF II) equiped with a 20 kV $Ar_{2,500+}$ gas cluster ion beam. The etching rate was ≈10 nm min^{-1} on SiO_2 reference.

Note S1

Initially, we carried out the plasma at different atmosphere and figure out that the sequence of O_2-Ar-O_2 plasma treatment (OAO) shows the best electrochemical properties in terms of cycling stability (**Figure S9**). Ar-LCO shows higher initial capacity but less stable during cycling, while O_2-LCO shows enhanced stability. It is believed that oxygen plasma would oxidize the sample, which leads to the phase change at the surface, while argon plasma would bring away

the oxygen, which introduce oxygen vacancy in the surface. Therefore, through the sequential O_2-Ar-O_2 plasma, the surface of LCO would be reconstructed to trilayer surface. This is confirmed by the STEM in Figure 3b. The interface is cation-disorder through Ar plasma while the surface is rocksalt structure with good lattice coherency with the bulk phase through O_2 plasma. Therefore, this sequence is set as most favorable condition for LCO stability. The plasma time is then optimized ranging from 30 to 1800 s, while the plasma power is also tested at 80 and 150 W**(Figure S10** and **Figure S11)**. It is found that suitable plasma time and power (90 s and 120 W, respectively), which is expected to have strong influence on the thickness of the pre-fatigued layer, is crucial in stabilizing the LCO.

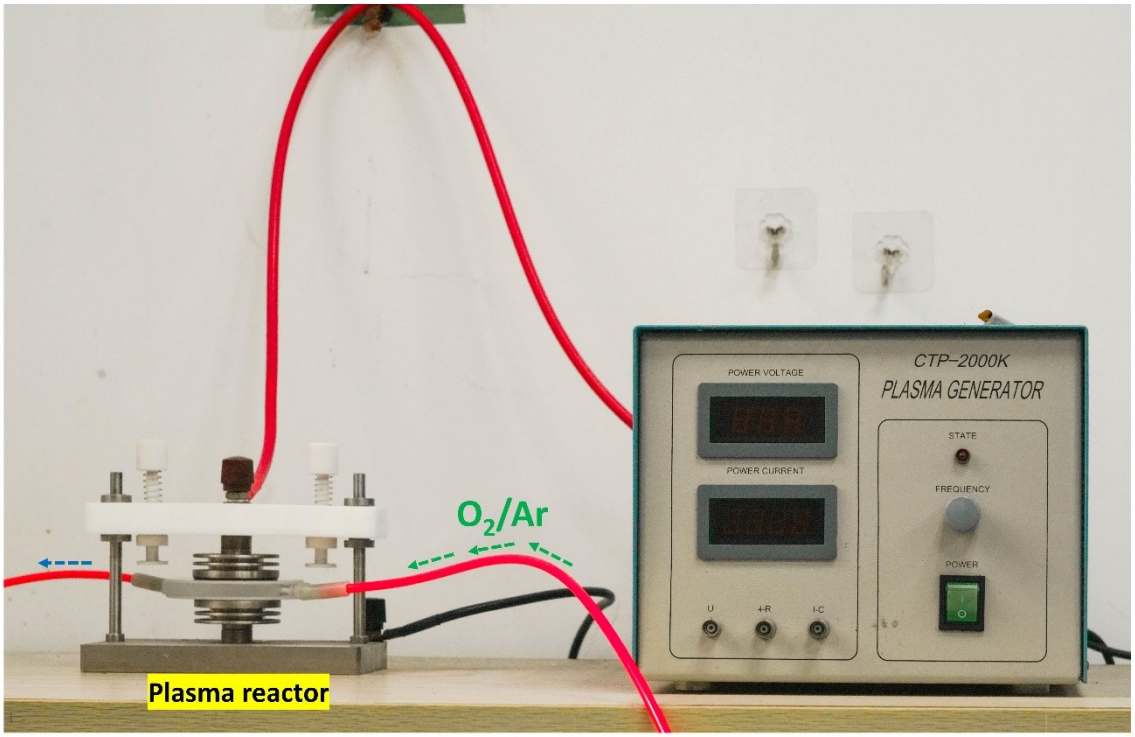

Figure S1. Image of plasma generator and plasma reactor.

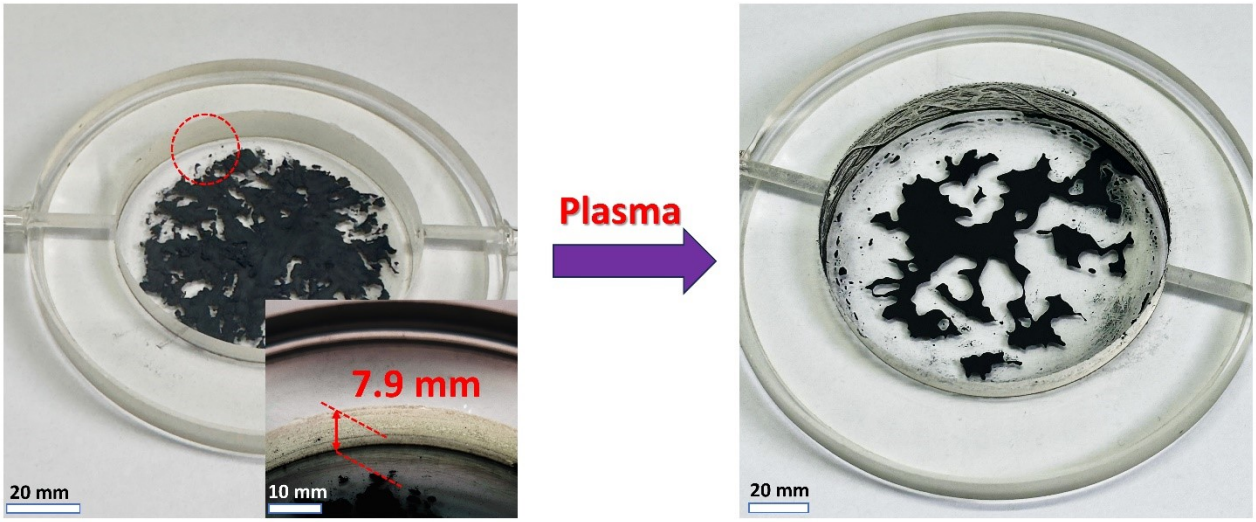

Figure S2. Image of the LCO before and after plasma treatment

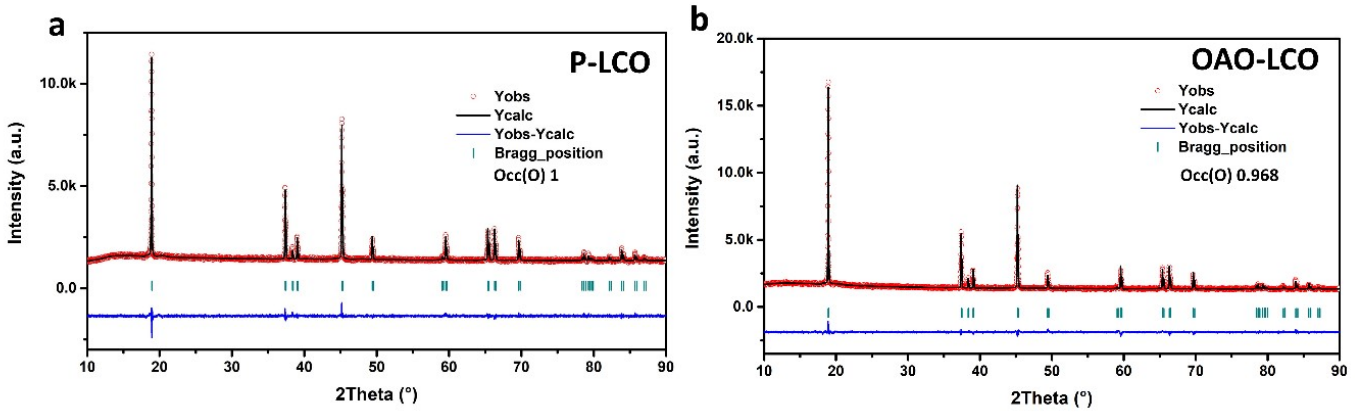

Figure S3. XRD patterns and the corresponding refinement results of LCO and OAO-LCO

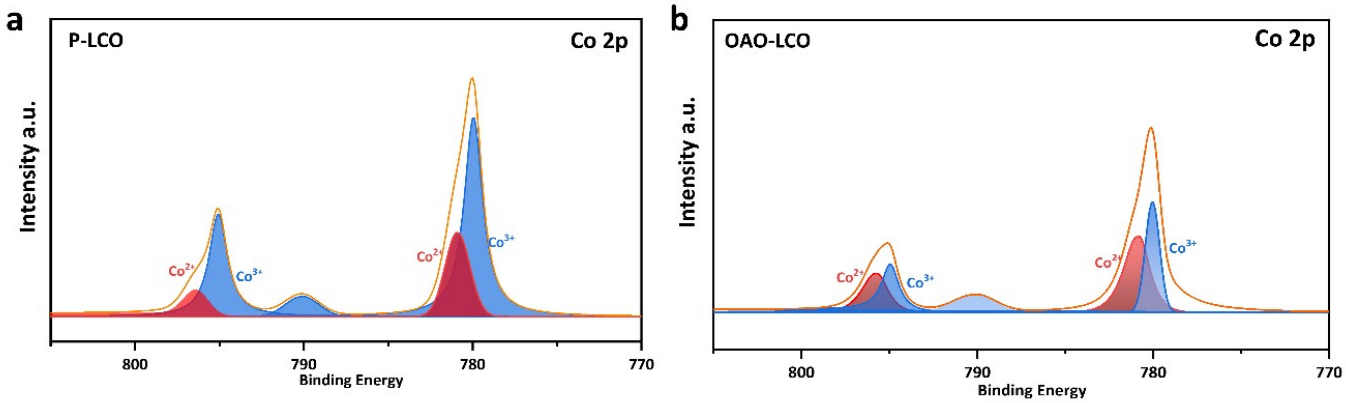

Figure S4. The Co *2p* XPS spectra of P-LCO and OAO-LCO

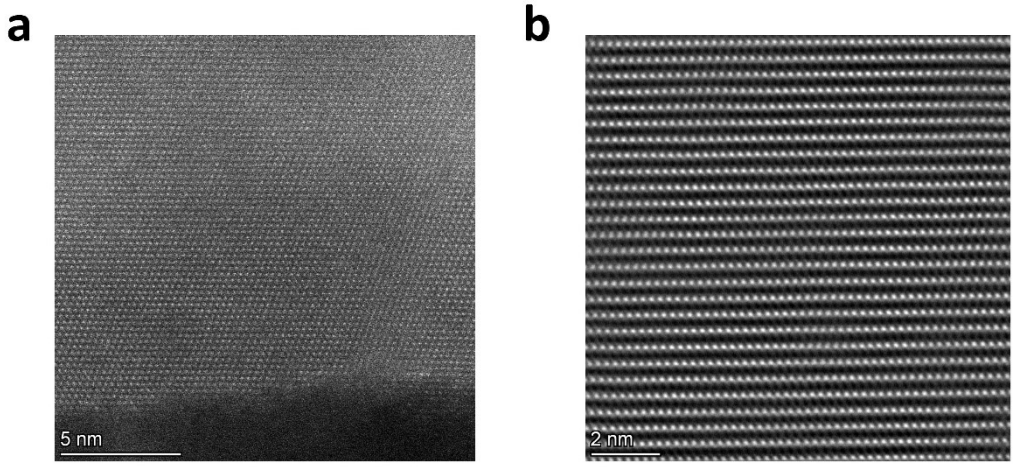

Figure S5. HAADF-STEM images of Bulk Part for OAO-LCO samples

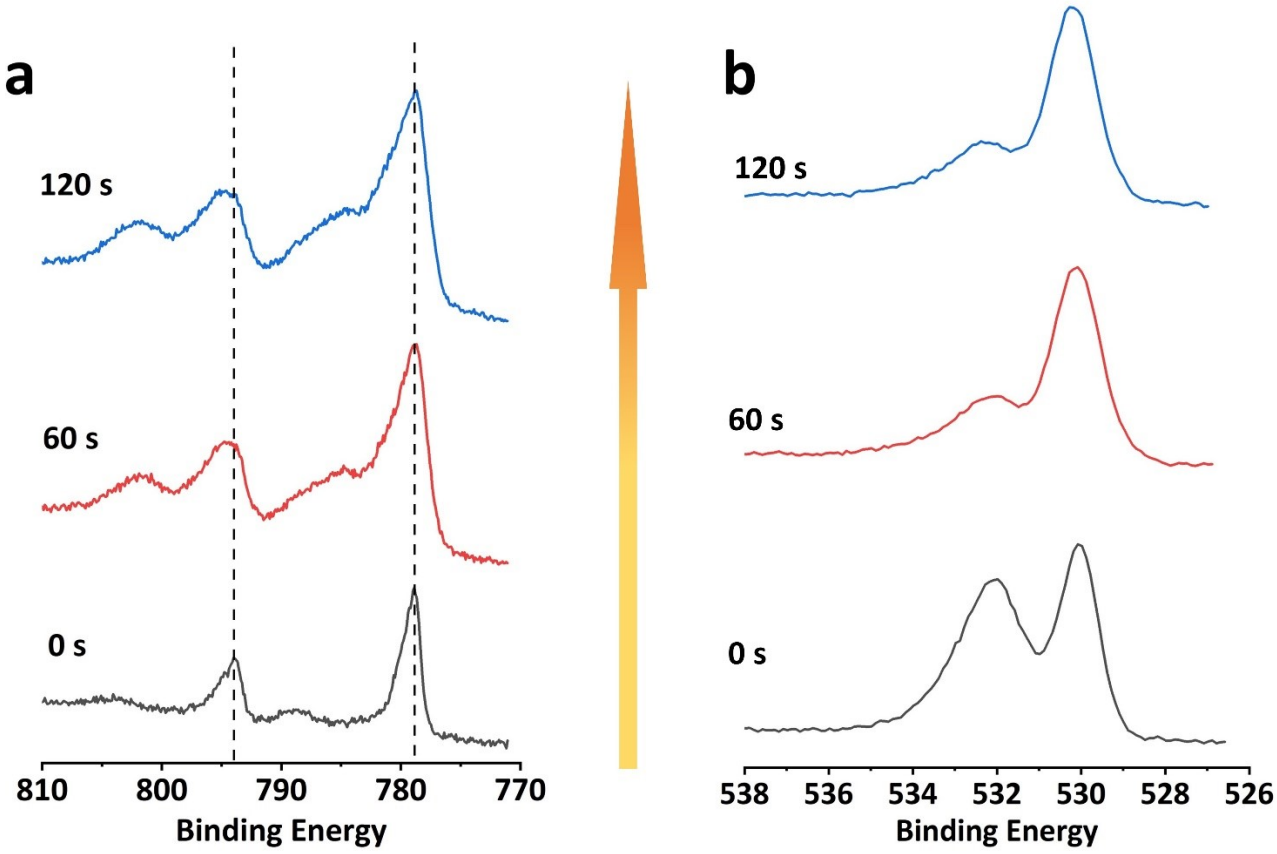

Figure S6. The a) Co *2p* and b) O*1s* XPS spectra of OAO-LCO after argon ion etching.

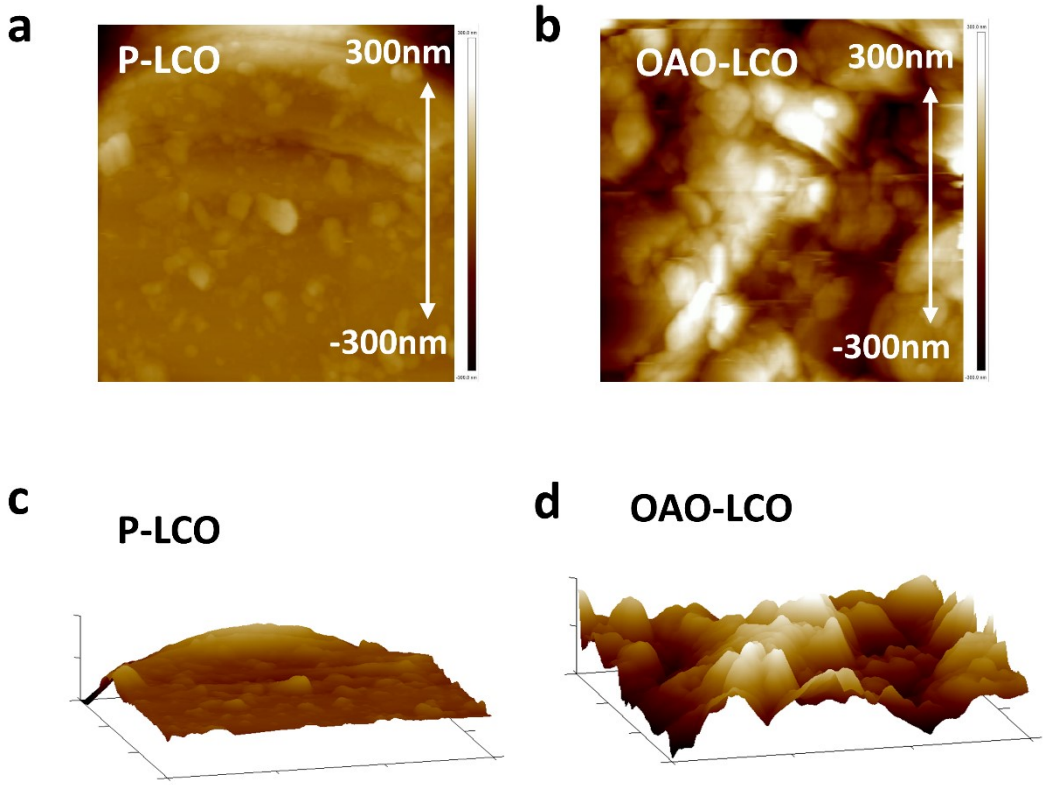

Figure S7. AFM Height images and 3d-images of a,c) P-LCO and b,d) OAO-LCO.

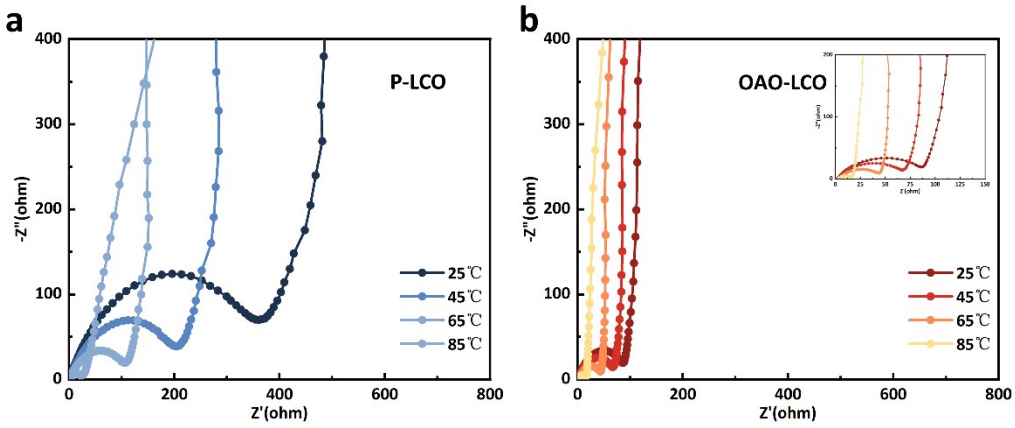

Figure S8. Nyquist plots of a) P-LCO and b) OAO-LCO cells before cycle at 25 °C,45 °C,65 °C,85°C

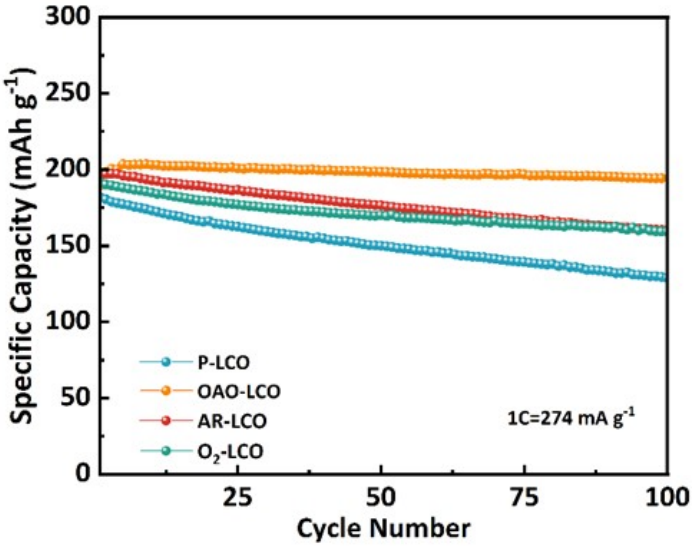

Figure S9. The cyclic performance of P-LCO ,AR-LCO ,O_2-LCO and OAO-LCO within 3.0–4.6 V at 1C

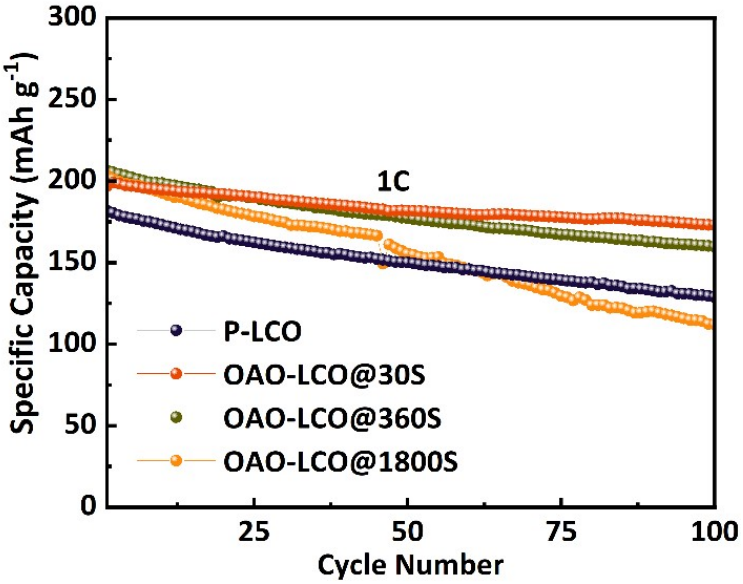

Figure S10. The cyclic performance of P-LCO , OAO-LCO@30s, OAO-LCO@360s and OAO-LCO@1800s within 3.0–4.6 V at 1C (OAO-LCO@30s, OAO-LCO@360s and OAO-LCO@1800s refer to plasma treatment total time of 30, 360, and 1800s, which means single atmosphere treatment time of 10, 120, and 600 s, respectively.).

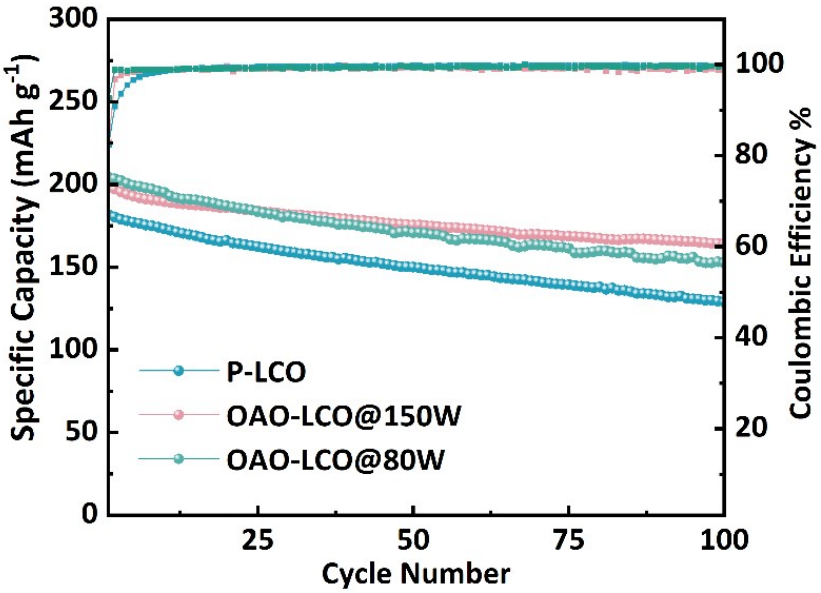

Figure S11. The cyclic performance of P-LCO , OAO-LCO@150w, and OAO-LCO@80w within 3.0–4.6 V at 1C. (OAO-LCO@150w, and OAO-LCO@80w refers to plasma power of 150 and 80 W, respectively.)

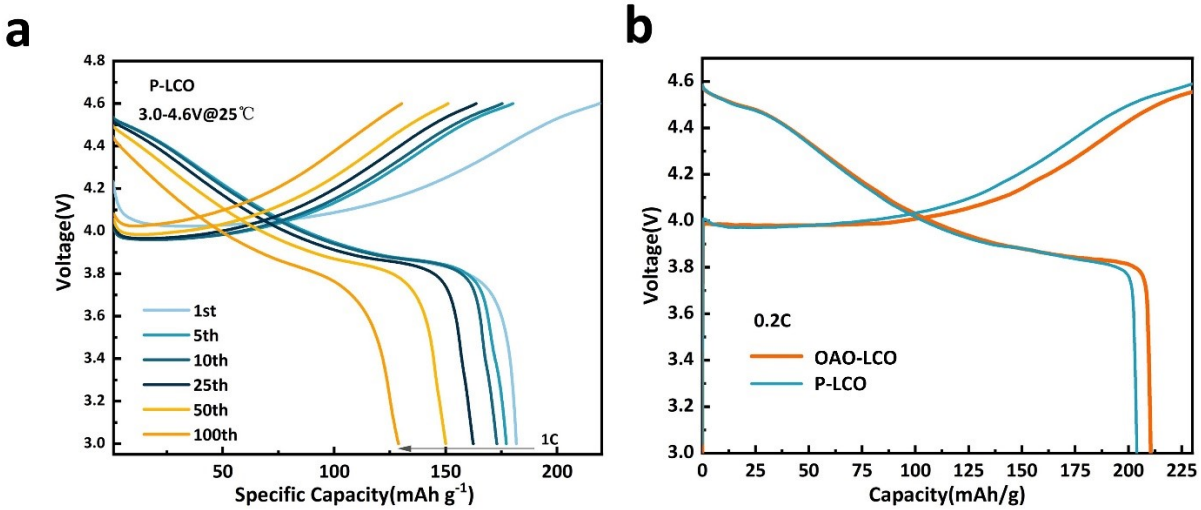

Figure S12. a)The charge/discharge curves for P-LCO of different cycle numbers. b) The charge/discharge curves for P-LCO and OAO-LCO of 1st cycle at 0.2C

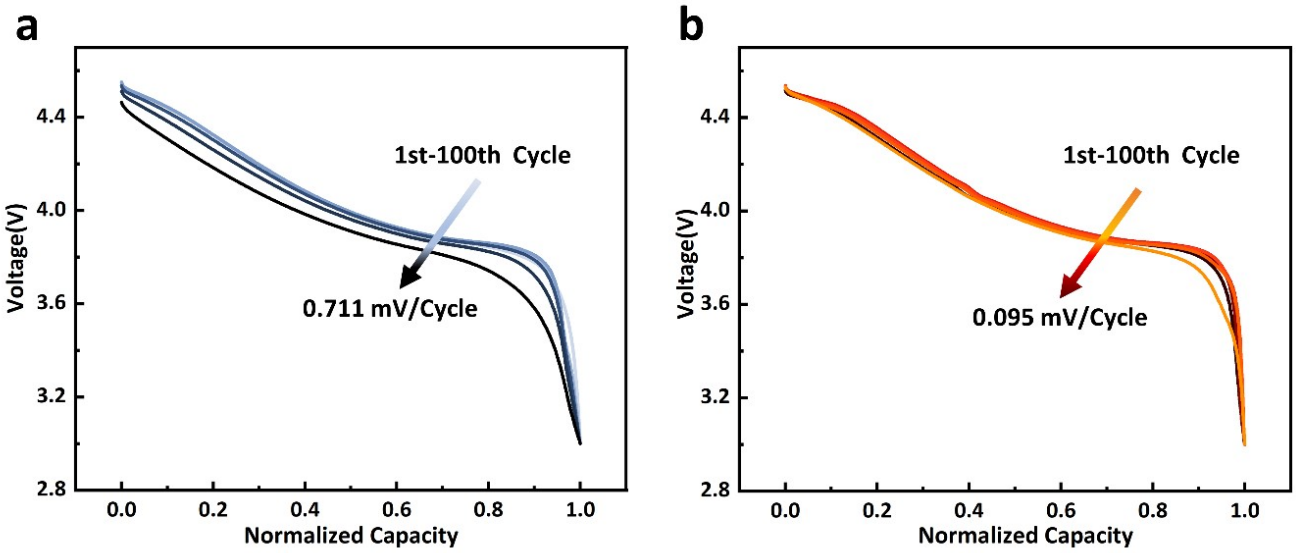

Figure S13. The variation of discharge curves upon cycling at 1 C for the a) P-LCO and b) OAO-LCO cathodes.

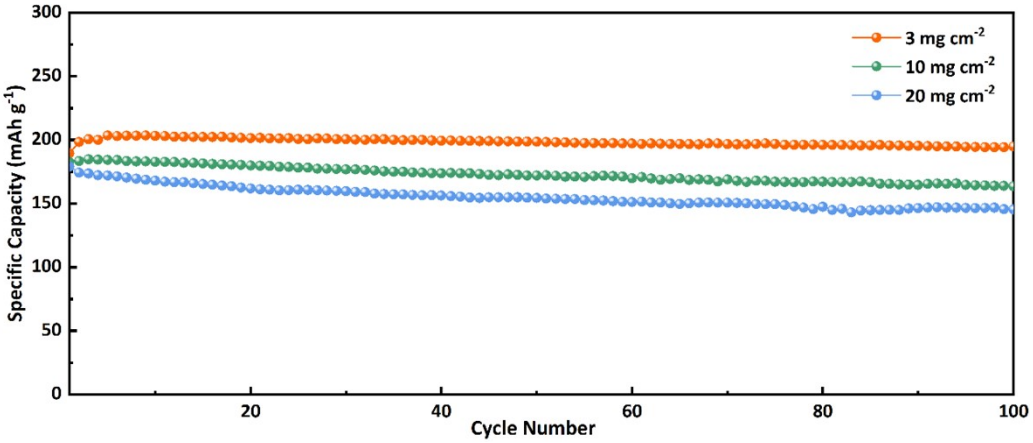

Figure S14. Electrochemical performance of the OAO-LCO at high-loading.

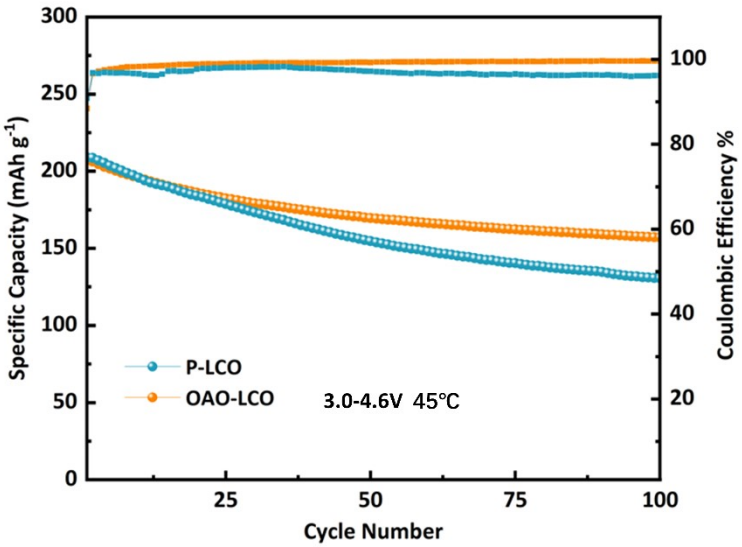

Figure S15. The cyclic performance in the range of 3.0–4.6 V at elevated temperature of 45 °C.

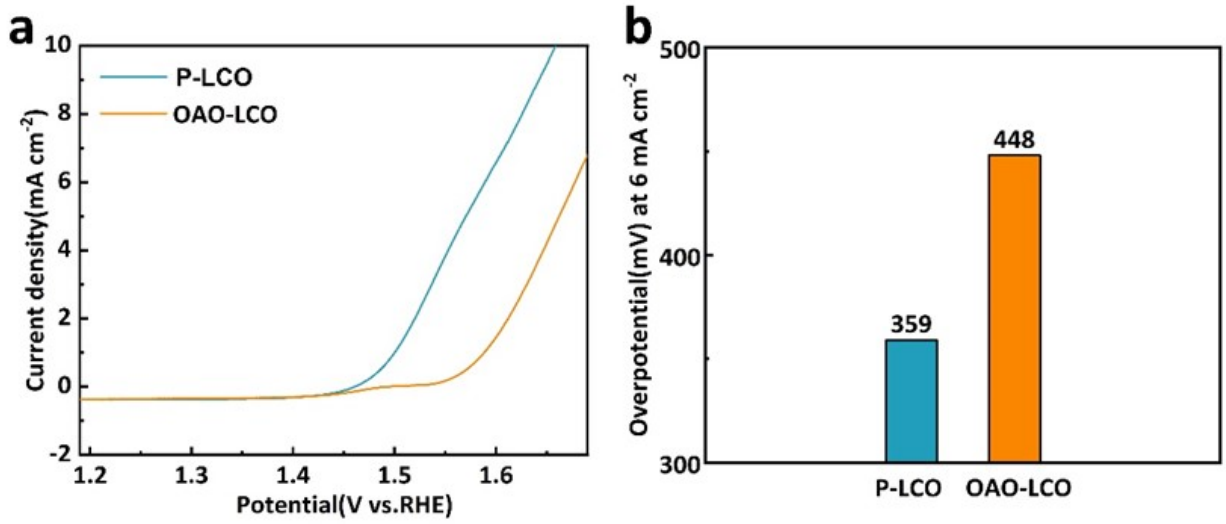

Figure S16. OER electrocatalytic performance for of P-LCO, and OAO-LCO in 0.1 M KOH aqueous solution at room temperature. (a) Linear sweep voltammetry (LSV) curves at a scan rate of 10 mV s^{-1} . Voltages are vs. reversible hydrogen electrode (RHE). (b) Measured overpotential at 6 mA cm^{-2} current density

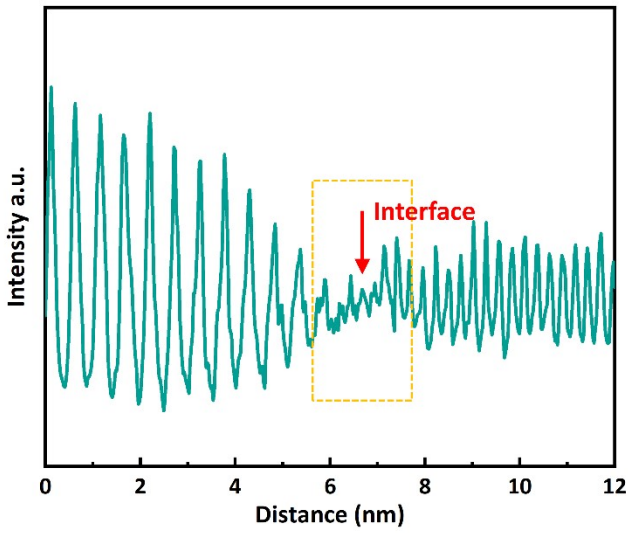

Figure S17. The line scan pattern for OAO-LCO after 50 cycles

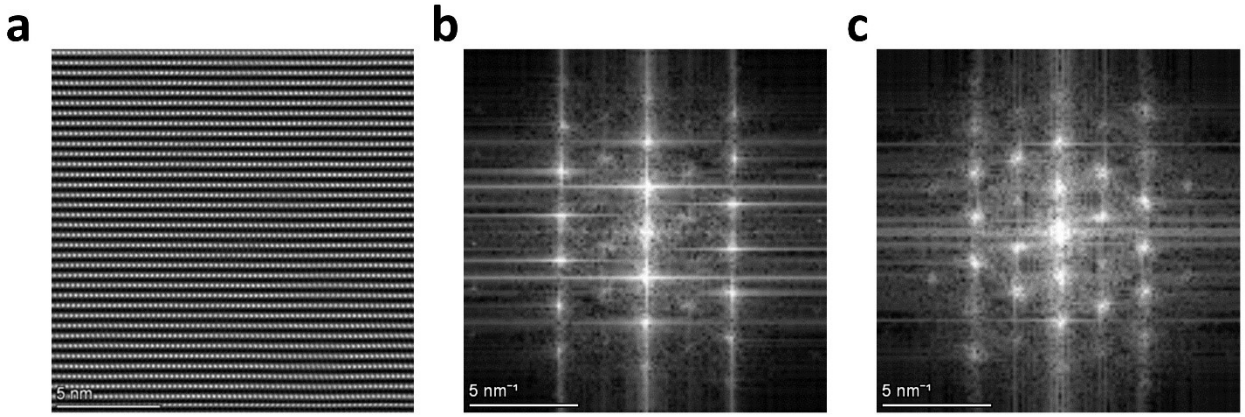

Figure S18. a) HAADF-STEM images of bulk part for OAO-LCO samples after 50 cycles. FFT patterns of HAADF-STEM images of b)Bulk Part and c) surface part for OAO-LCO samples

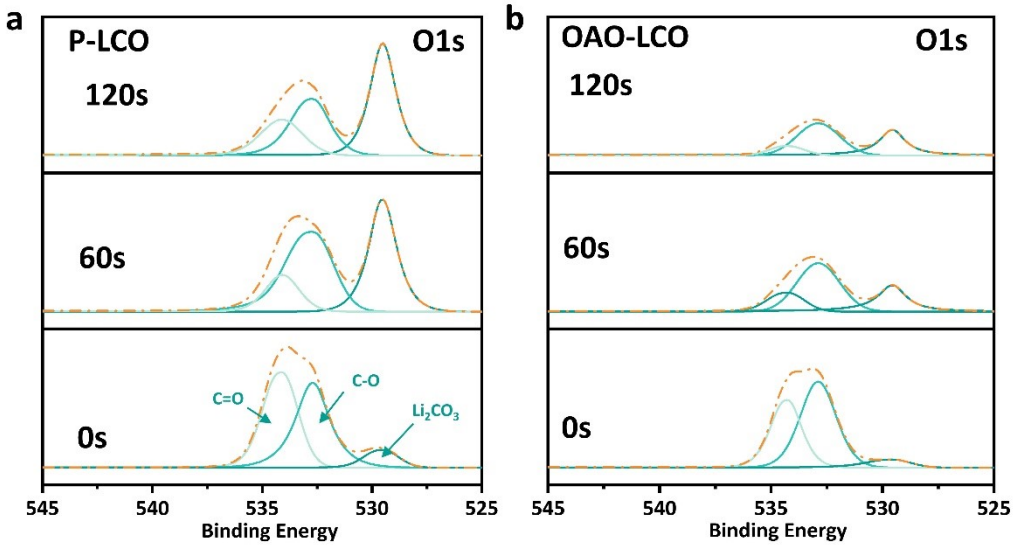

Figure S19. The O1s XPS spectra of the a) P-LCO and b) OAO-LCO cathode after 50th cycle.

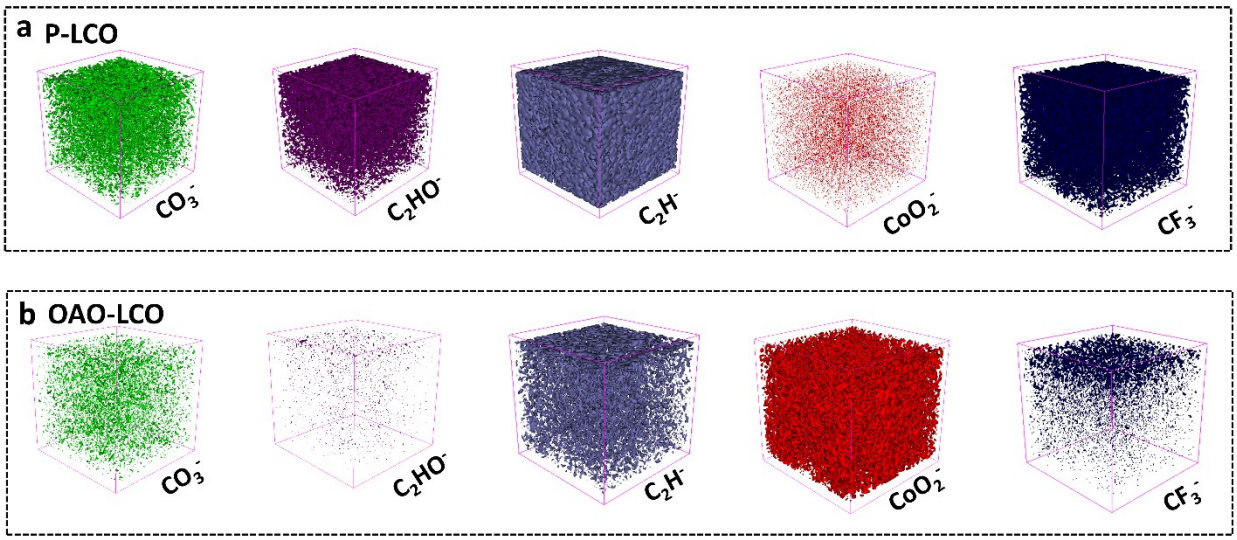

Figure S20. The TOF-SIMS 3D reconstruction of CoO_2^-, CO_3^-, C_2H^-, CF_3^- and C_2HO^- fragments of a) P-LCO and b) OAO-LCO.

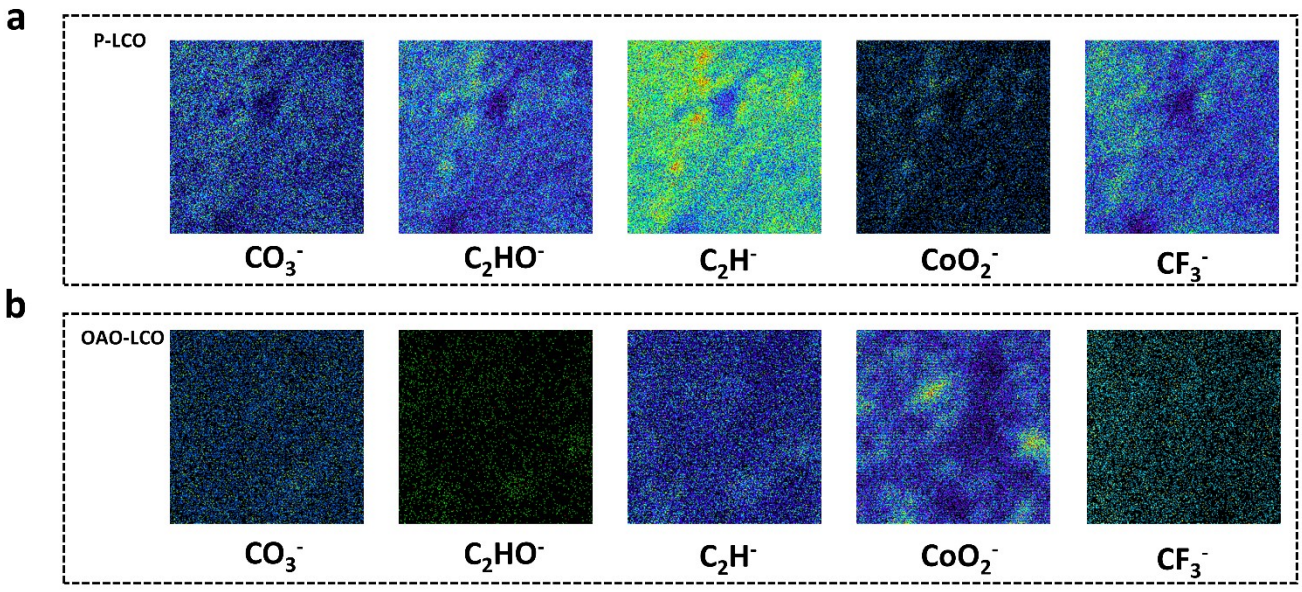

Figure S21. The TOF-SIMS vertical signals integration of CoO_2^-, CO_3^-, C_2H^-, CF_3^- and C_2HO^- fragments of a) P-LCO and b) OAO-LCO.

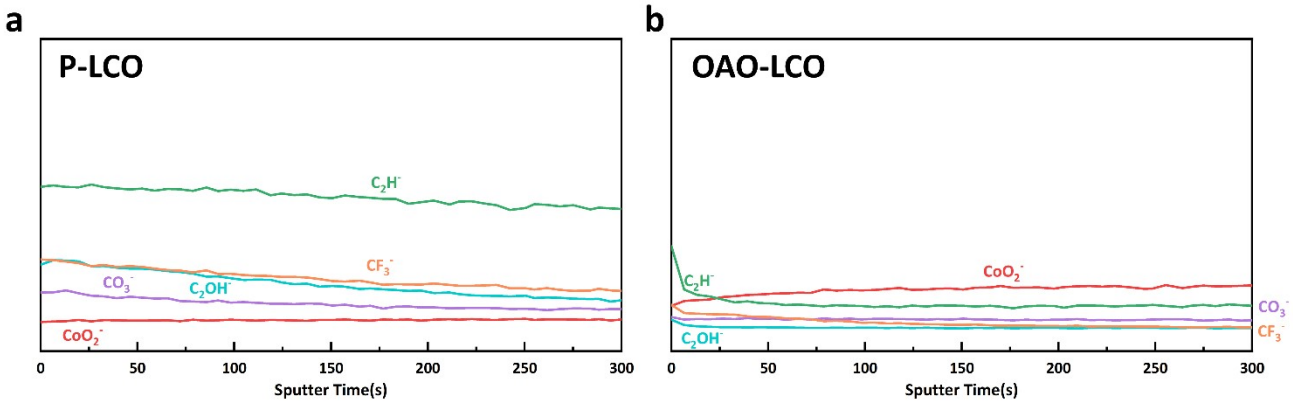

Figure S22. The TOF-SIMS depth profiling of CoO_2^-, CO_3^-, C_2H^-, CF_3^- and C_2HO^- fragments of a) P-LCO and b)OAO-LCO.

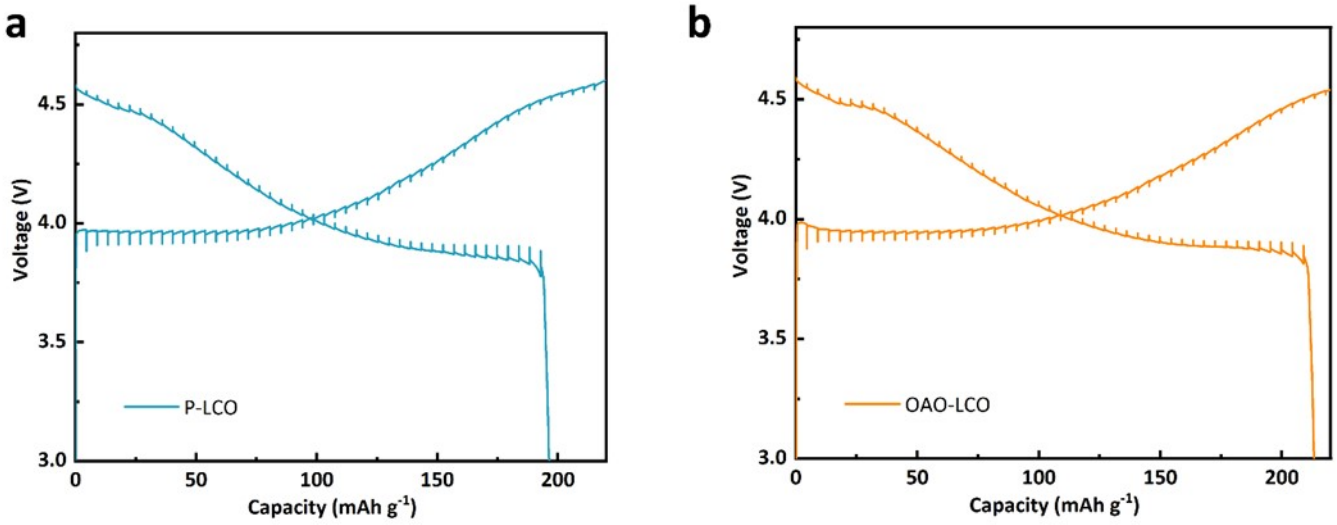

Figure S23. GITT measurements of a) P-LCO and b) OAO-LCO during the initial charge/discharge.

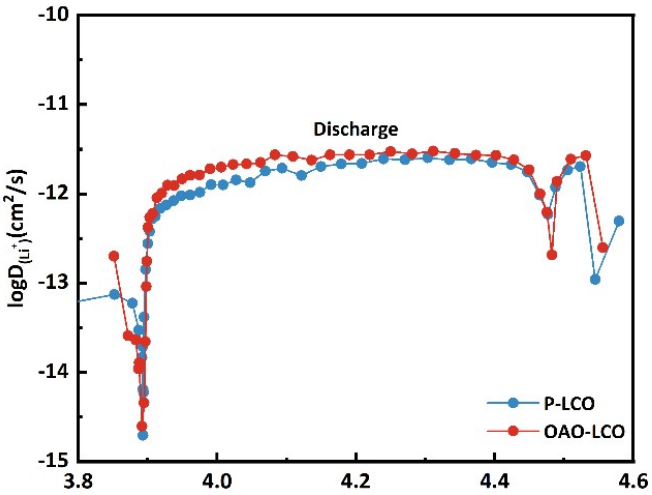

Figure S24. The Li^+ diffusivity within the P-LCO and OAO-LCO cathodes at the state of discharge in the first cycle calculated from GITT

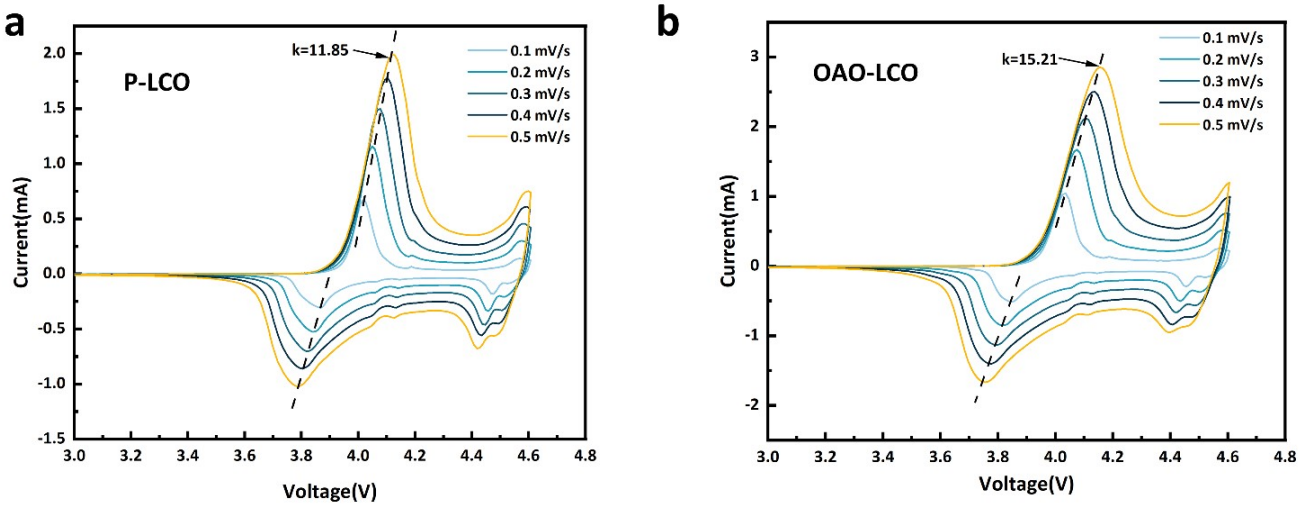

Figure S25. CV curves of a) P-LCO and b) OAO-LCO at different scan rates.

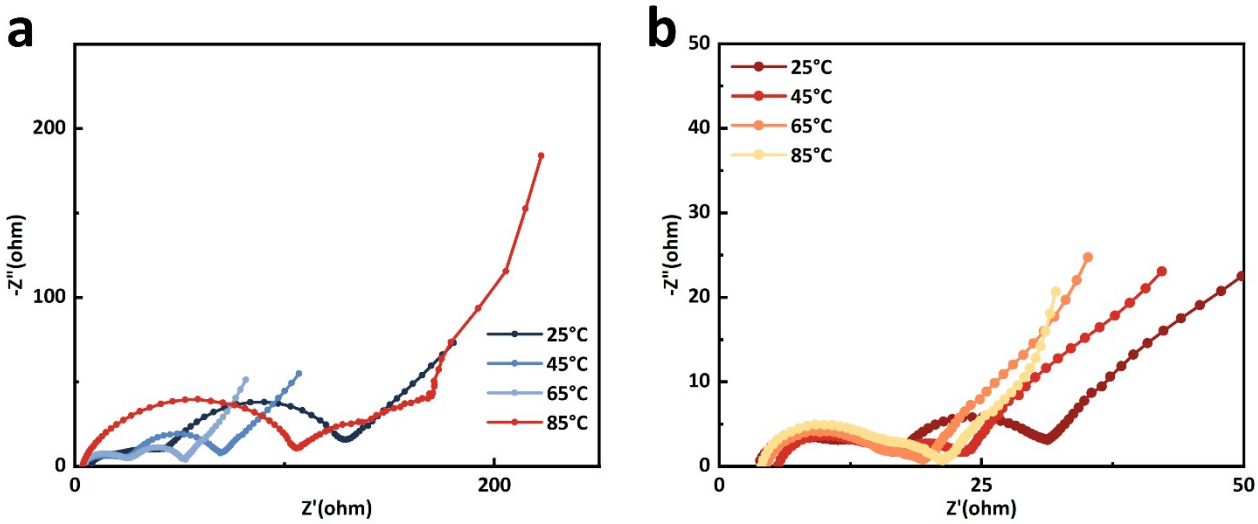

Figure S26. The magnified Nyquist plots of a) P-LCO and b) OAO-LCO cells after 50 cycles at 25ºC,45ºC,65ºC and 85ºC.

Table S1. The crystallographic parameters of P-LCO and OAO-LCO from XRD Rietveld refinements

Parameters	P-LCO	OAO-LCO
a (Å)	2.817535	2.816705
b(Å)	2.817535	2.816705
c(Å)	14.06694	14.06328
Volume($Å^3$)	96.7094	96.6273
Rp	1.79%	1.76%
Rwp	2.34 %	2.24%

Table S2. The crystallographic parameters of P-LCO and OAO-LCO from NPD Rietveld refinements

Parameters	P-LCO	OAO-LCO
a (Å)	2.819707	2.819450
b(Å)	2.819707	2.819450
c(Å)	14.083410	14.082013
Volume($Å^3$)	96.972	96.945
Rwp	4.52%	4.86%

Table S3 Comparison of the initial capacity of reported LiCoO2

Capacity (mAh g^{-1})	Rate (C)	Nominal specific capacity	Cycle life	Capacity retention	Reference
111.1	5	1C=274 mAh g^{-1}			1
~135	3	1C=274 mAh g^{-1}			2
110	10	1C=274 mAh g^{-1}			3
71	3	1C=274 mAh g^{-1}			4
~120	5	1C=274 mAh g^{-1}			5
~150	4	1C=270 mAh g^{-1}			6
~120	4	1C=274 mAh g^{-1}			7
~125	5	1C=280 mAh g^{-1}			8
~100	5	1C=270 mAh g^{-1}			9
~148	10	1C=270 mAh g^{-1}			10

~180	1	1C=280 mAh g-1	600	70%	11
150	**10**	**1C=274 mAh g^{-1}**	**1000**	**89%**	**This work**

References

1. C. Sun, B. Zhao, J. Mao, K. H. Dai, Z. y. Wang, L. b. Tang, H. z. Chen, X. h. Zhang and J. c. Zheng, *Adv. Funct. Mater.*, 2023, **33**.
2. S. L. Mao, Z. Y. Shen, W. D. Zhang, Q. Wu, Z. Y. Wang and Y. Y. Lu, *Adv. Sci.*, 2022, **9**, 10.
3. N. Qin, Q. M. Gan, Z. F. Zhuang, Y. F. Wang, Y. Z. Li, Z. Q. Li, H. Iftikhar, C. Zeng, G. Y. Liu, Y. F. Bai, K. L. Zhang and Z. G. Lu, *Adv. Energy Mater.*, 2022, **12**, 11.
4. J. W. Qian, L. Liu, J. X. Yang, S. Y. Li, X. Wang, H. L. L. Zhuang and Y. Y. Lu, *Nat. Commun.*, 2018, **9**, 11.
5. Y. Wang, Q. H. Zhang, Z. C. Xue, L. F. Yang, J. Y. Wang, F. Q. Meng, Q. H. Li, H. Y. Pan, J. N. Zhang, Z. Jiang, W. L. Yang, X. Q. Yu, L. Gu and H. Li, *Adv. Energy Mater.*, 2020, **10**, 10.
6. Y. Y. Huang, Y. C. Zhu, H. Y. Fu, M. Y. Ou, C. C. Hu, S. J. Yu, Z. W. Hu, C. T. Chen, G. Jiang, H. K. Gu, H. Lin, W. Luo and Y. H. Huang, *Angew. Chem. Int. Ed.*, 2021, **60**, 4682-4688.
7. C. Yang, X. B. Liao, X. Zhou, C. L. Sun, R. Qu, J. Han, Y. Zhao, L. G. Wang, Y. You and J. Lu, *Adv. Mater.*, 2023, **35**, 9.
8. F. C. Zhang, N. Qin, Y. Z. Li, H. Guo, Q. M. Gan, C. Zeng, Z. Q. Li, Z. Y. Wang, R. Wang, G. Y. Liu, S. Gu, H. Huang, Z. L. Yang, J. Wang, Y. H. Deng and Z. G. Lu, *Energy Environ. Sci.*, 2023, **16**, 4345-4355.
9. W. J. Kong, D. Wong, K. An, J. C. Zhang, Z. H. Chen, C. Schulz, Z. J. Xu and X. F. Liu, *Adv. Funct. Mater.*, 2022, **32**, 11.
10. M. Z. Cai, Y. H. Dong, M. Xie, W. J. Dong, C. L. Dong, P. Dai, H. Zhang, X. Wang, X. Z. Sun, S. N. Zhang, M. Yoon, H. W. Xu, Y. S. Ge, J. Li and F. Q. Huang, *Nat. Energy*, 2023, **8**, 159-+.
11 F. Zhang, N. Qin, Y. Li, H. Guo, Q. Gan, C. Zeng, Z. Li, Z. Wang, R. Wang, G. Liu, S. Gu, H. Huang, Z. Yang, J. Wang, Y. Deng a and Z. Lu, *Energy Environ. Sci.*, 2023, **16**, 4345-4355

\